The Astronomical Journal, 131:3100–3108, 2006 June

MEASUREMENTS OF BINARY STARS, INCLUDING TWO NEW DISCOVERIES, WITH THE LICK OBSERVATORY ADAPTIVE OPTICS SYSTEM

Julian C. Christou
Center for Adaptive Optics, University of California, 1156 High Street, Santa Cruz, CA 95064; christou@ucolick.org

and

Jack D. Drummond
Starfire Optical Range, Directed Energy Directorate, Air Force Research Laboratory, Kirtland AFB NM 87117-5776
Received 2005 December 1; accepted 2006 January 28

ABSTRACT

We present astronomical results from observations for a number of multiple star systems observed with the Lick Observatory natural guide star adaptive optics system. We have discovered and classified a fifth component in the ι Cas system and a third component for the wide binary WDS 00310+2839. Using two different data reduction techniques, we demonstrate relative astrometric precision to 2–3 mas and photometric precision to within 0.05 mag. The binary stars enable anisoplanatism to be measured, from which a mean turbulence height over Lick Observatory of 1.5–3 km is determined.

Key words: astrometry — binaries: close — instrumentation: adaptive optics — techniques: photometric

1. INTRODUCTION

During an observing run in 2004 August to image asteroids with the Lick Observatory adaptive optics (AO) system (J. D. Drummond & J. C. Christou 2006, in preparation), data sets were also obtained for several binary and multiple stars (preliminary results presented in Christou & Drummond 2005). The majority of these objects were observed as calibration targets for the asteroids to check the spatial scale and orientation of the camera. Two of them were observed for their astronomical interest. These were the multiple system ι Cas, previously known to have four components (Drummond et al. 2003), and the wide binary WDS 00310+2839, for which a third companion had been discovered during a previous AO run in 2003 September (J. C. Christou 2003, unpublished). From these observations a previously unknown fifth component to ι Cas, a companion to the C component, was detected, and the presence of the third component of WDS 00310+2839 was confirmed. In keeping with tradition, we give these two new companions a discovery designation of JCD-1 for WDS 00310+2839 and JCD-2 for ι Cas c. Follow-up observations of both systems were obtained in 2005.

Roberts et al. (2005) point out that extracting photometry from AO imaging is problematic. For the results presented in this paper, we measured the astrometry and photometry using two different techniques previously demonstrated to be applicable to AO observations of multiple point sources (Drummond 1998; Barnaby et al. 2000; Christou et al. 2004a), making use of multiple observations. The final results were obtained by taking the average of those from the two techniques. From the multiband infrared differential photometry we computed blackbody curves to determine the spectral types of the new components.

In addition to the stellar photometry, astrometry, and classification, we have also been able to characterize the performance of the AO system by investigating the Strehl ratios of the binary components. These observations also permit us to measure the anisoplanatism between the components of the wide binaries. We have characterized the precision to which the relative astrometry can be computed, and these results illustrate the accuracy to which detectors should be calibrated for high spatial resolution observations.

2. OBSERVATIONS AND REDUCTIONS

The primary observations were obtained at the Lick Observatory 3 m Shane Telescope using the natural guide star (NGS) AO system (Bauman et al. 1999) with the IRCAL infrared imager (Lloyd et al. 2000) on the nights of 2004 August 28–30. The binary and multiple stars were observed in the near-infrared J, H, and K bands over the course of the three nights, interspersed with the asteroid observations. The seeing conditions were very good during the observing run, with coherence length r_0 (at 550 nm) values ranging from 8 to 18 cm. The AO performance is typically characterized by the Strehl ratio, with perfect performance, i.e., no aberrations in the optical system, having a value of 100%. The measured K-band Strehl ratios for a number of point-source stars throughout the run ranged from 30% to 60%. A more detailed discussion of the Strehl ratio calculation is in § 4.

The calibration binary stars σ CrB, γ Del, 70 Oph, and μ Cas were all observed in the K band with a Brackett gamma (Brγ) filter we label K(Brγ) ($\lambda_0 = 2.167$ μm; $\Delta\lambda = 0.020$ μm). In addition, both σ CrB and μ Cas were also observed in the J band, with the former using a broadband filter ($\lambda_0 = 1.238$ μm; $\Delta\lambda = 0.271$ μm) and the latter a narrowband filter J' ($\lambda_0 = 1.183$ μm; $\Delta\lambda = 0.040$ μm). The two multiple systems, WDS 00310+2839 and ι Cas, were observed in all three bands, K_s ($\lambda_0 = 2.150$ μm; $\Delta\lambda = 0.320$ μm), H ($\lambda_0 = 1.656$ μm; $\Delta\lambda = 0.296$ μm), and J ($\lambda_0 = 1.238$ μm; $\Delta\lambda = 0.271$ μm). Observations of WDS 00310+2839 in the K_s band were also obtained on 2003 September 9 and 2005 October 12, and ι Cas was observed again on 2005 August 19.

The nominal image scale for the IRCAL camera is $0\farcs076$ pixel^{-1}, so that the K-band observations are critically sampled with a theoretical resolution (λ/D) of $0\farcs149$. However, the J- and H-band images are both undersampled, with resolutions of $0\farcs085$ and

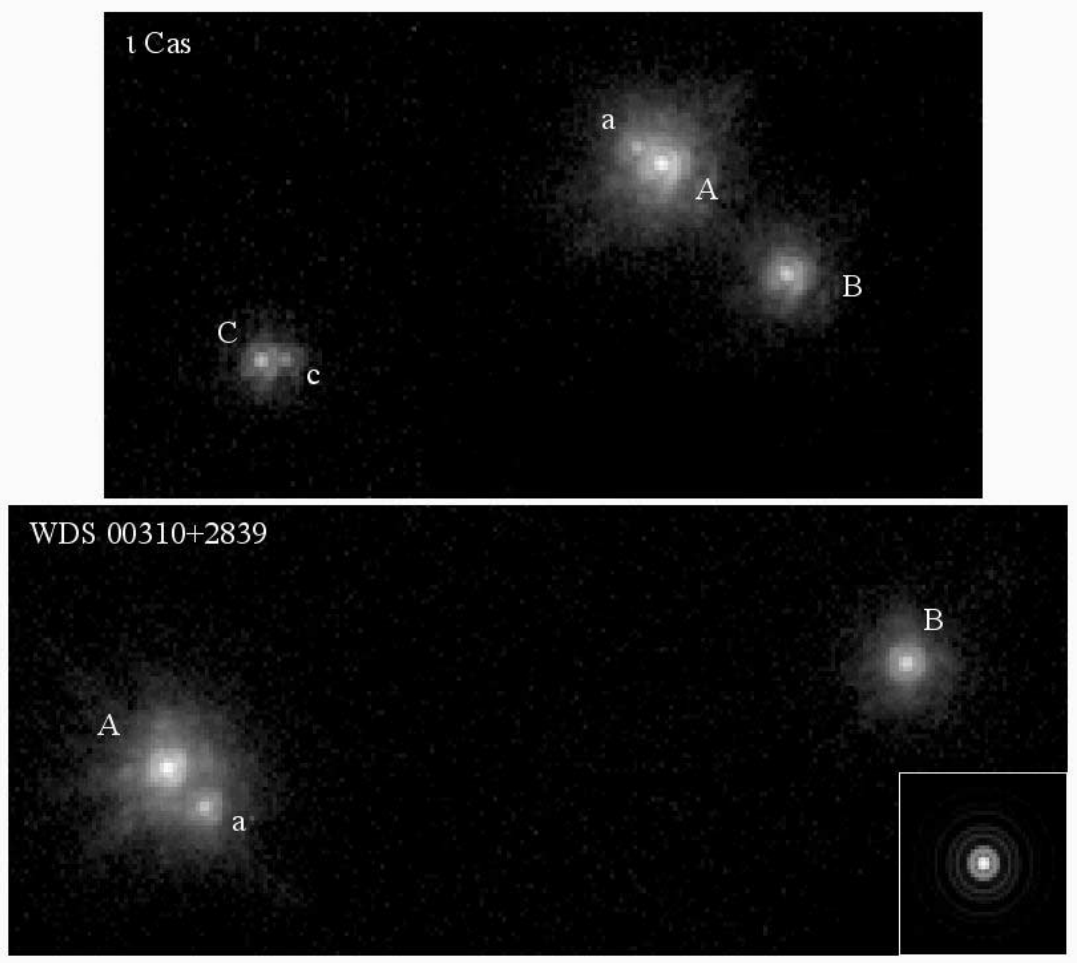

FIG. 1.—Sample *K*-band images of ι Cas (*top*) and WDS 00310+2839 (*bottom*) clearly identifying the multiple components. The inset shows the diffraction-limited PSF. All images are displayed on a logarithmic scale.

0.″114, respectively. Figure 1 shows single-frame *K*-band observations of ι Cas and WDS 00310+2839. The five components of the former are clearly visible, showing the binary nature of both the A and, for the first time, the C components. Similarly, the binary nature of WDS 00310+2839A is clearly seen. The diffraction-limited cores are clearly visible, as is the residual halo structure, due to the uncompensated components of the wave front. The effects of the spiders are also seen in the point-spread functions (PSFs). The close binaries clearly show the problem of measuring photometry in that the secondaries lie within the extended halo structure of the primary. The figures also show the strong degree of similarity in the structure between the widely separated PSFs discussed in detail in § 4.

Each set of observations consisted of a series of short exposures (0.057–10 s), which were initially preprocessed by sky subtraction. The astrometry and photometry of the stars were obtained by two independent methods, parametric blind deconvolution (PBD) and multiframe blind deconvolution (MFBD). Both techniques have been previously successfully applied to binary star, multiple star, and cluster AO observations (Drummond 1998; Barnaby et al. 2000; Christou et al. 2004b). PBD models each of the PSFs in the image as a two-dimensional elliptical Lorentzian profile, which has been found to be an appropriate model for AO images. For this application, a Lorentzian profile was fitted to each component in each of the separate frames. If the stars were separated by 1″ or less, then an isoplanatic assumption was made, i.e., the shapes of the Lorentzians were forced to be the same. For separations greater than 1″ this constraint was relaxed to take into account any PSF variability across the field, i.e., anisoplanatism. A weighted mean, with the weights coming from the uncertainties of the fits, was computed for the separation, position angle (P.A.), and magnitude difference (Δm) for the components. The PSFs in Figure 1 show departures from a Lorentzian model in that Airy rings are clearly visible. We compared the relative photometry and astrometry obtained from a Lorentzian fit to those obtained from a combined Lorentzian and Airy function fit for one of the ι Cas data sets and found that they remain unchanged (within the dispersion of the measurements), justifying using the simpler parametric model.

By comparison, MFBD finds a common solution to a set of independent images of the same field, assuming that the PSF varies from one frame to the next. The series of observations was broken into smaller subsets, typically four per set of observations, and a deconvolved image was computed with each component constrained to have a Gaussian shape at the end. The relative astrometry and photometry were computed by two-dimensional elliptical Gaussian fits to these deconvolved images. As for PBD, the weighted mean of the separation, P.A., and Δm were computed.

The final parameters were obtained by taking the unweighted mean and standard deviation of the PBD and MFBD results. The unweighted mean minimizes the effect of any systematic errors in one or the other of the two independent methods by favoring neither of them. Table 1 shows these final measurements for the

TABLE 1
BINARY STAR RESULTS

NAME	V_A	V_B	DATE	P.A. (deg)	SEPARATION (arcsec)	Δm		
						J (1.238 μm)	H (1.656 μm)	K_s (2.150 μm)
σ CrB	5.62	6.49	2004 Aug 28.90	237.5 ± 0.1	7.032 ± 0.008	0.83 ± 0.34	...	1.01 ± 0.01[a]
70 Oph	4.22	6.20	2004 Aug 29.15	137.4 ± 0.1	4.785 ± 0.004	...	...	0.80 ± 0.09[a]
γ Del	4.36	5.03	2004 Aug 28.34	266.2 ± 0.1	9.224 ± 0.003	...	...	2.08 ± 0.04[a]
μ Cas	5.14	11.45	2004 Aug 30.22	65.0 ± 1.3	1.042 ± 0.020	5.21 ± 0.16[b]	...	4.072 ± 0.31[a]
ι Cas	...	...	2004 Aug 28.99	...	...	...	...	...
Aa	...	...	...	57.1 ± 0.2	0.485 ± 0.005	2.45 ± 0.15	2.13 ± 0.01	2.15 ± 0.13
AB	4.65	6.87	...	230.6 ± 0.1	2.735 ± 0.001	1.45 ± 0.02	1.25 ± 0.01	1.22 ± 0.01
AC	...	...	...	114.6 ± 0.1	7.433 ± 0.001	2.75 ± 0.01	2.35 ± 0.06	2.22 ± 0.01
Ac	...	...	...	115.8 ± 0.1	7.059 ± 0.001	4.60 ± 0.07	4.01 ± 0.10	3.84 ± 0.02
Cc	...	...	...	272.1 ± 0.4	0.405 ± 0.005	1.85 ± 0.06	1.67 ± 0.04	1.62 ± 0.01
	...	...	2005 Aug 19.42	...	...	...	...	...
Aa	...	...	...	55.2 ± 0.3	0.510 ± 0.003	...	...	2.07 ± 0.03
AB	...	...	...	232.1 ± 0.1	2.735 ± 0.001	...	...	1.25 ± 0.02
AC	...	...	...	116.0 ± 0.1	7.384 ± 0.006	...	...	2.23 ± 0.15
Ac	...	...	...	117.2 ± 0.8	7.031 ± 0.015	...	...	3.79 ± 0.21
Cc	...	...	...	273.0 ± 0.8	0.385 ± 0.008	...	...	1.55 ± 0.07
WDS[c]	...	...	2003 Sep 9.44	...	...	...	...	...
AB	11.64	11.81	...	277.7 ± 0.1	12.571 ± 0.001	...	...	1.28 ± 0.01
Aa	...	...	...	225.6 ± 0.1	0.879 ± 0.001	...	...	1.73 ± 0.07
	...	...	2004 Aug 19.18	...	...	...	...	...
AB	...	...	...	277.6 ± 0.1	12.554 ± 0.001	0.94 ± 0.02	1.21 ± 0.02	1.25 ± 0.02
Aa	...	...	...	225.6 ± 0.1	0.877 ± 0.002	1.58 ± 0.02	1.75 ± 0.03	1.77 ± 0.01
	...	...	2005 Oct 12.20	...	...	...	...	...
AB	...	...	...	278.9 ± 0.4	12.543 ± 0.006	...	...	1.23 ± 0.03
Aa	...	...	...	226.2 ± 0.4	0.873 ± 0.003	...	...	1.82 ± 0.10

[a] K (Brγ) (2.167 μm).
[b] J' (1.183 μm).
[c] WDS 00310+2839.

calibration binaries and the multiple stars. The astrometry from the two techniques agrees well, typically to within a few milliarcseconds, with a couple of exceptions (μ Cas and WDS 00310+2839AB), indicating that we are able to determine the relative positions of the stars to within 3% of the diffraction limit. Comparison of the calibration binaries to their orbits confirms the global plate scale of 76 mas pixel^{-1}, although we measured systematic differences in plate scale depending on chip location (see § 5). The magnitude differences have been determined to well within a few tenths, with a couple of exceptions (μ Cas and σ CrB in the J band). Figure 2 illustrates the similarity of the magnitude differences from the two methods for the components of ι Cas for the 2004 data. The filled symbols represent the MFBD fits to the individual frames, while the open symbols represent the PBD fits to five-frame subsets. It is interesting to note that these results show behavior similar to binary star photometry obtained from other systems in that the differential magnitudes show significant variation (Roberts et al. 2005). In some cases, the variation is different for the different reduction techniques, indicating the intrinsic scatter between the methods, but in some cases the two methods both track the variations. Roberts et al. (2005) suggest that scintillation and anisoplanatism can be contributing factors. The reduction techniques used here should minimize the effect of the latter, since spatially variant PSFs are allowed. Scintillation may have an effect in that some integration times are relatively short (57 ms per frame), essentially freezing the K-band compensation. However, there are also other possible sources of photometric error, such as residual flat-fielding errors, the location of the sources on the detector, and intrapixel sensitivity variations that can also contribute at the ~0.01–0.05 mag level (Lauer 1999; Mighell 2005).

The discovery of the c component for ι Cas prompted us to revisit the 2002 I-band 3.67 m telescope data (Drummond et al. 2003). With careful selection of the data for the best Strehl observations we have a marginal detection with a P.A. of ~271° and a separation of ~0.″42, slightly greater than the 2004 and 2005 data (Table 1), suggesting that the Cc components are closing. By comparison, the three measurements of the WDS 00310+2839 system, from 2003 to 2005, show no discernible

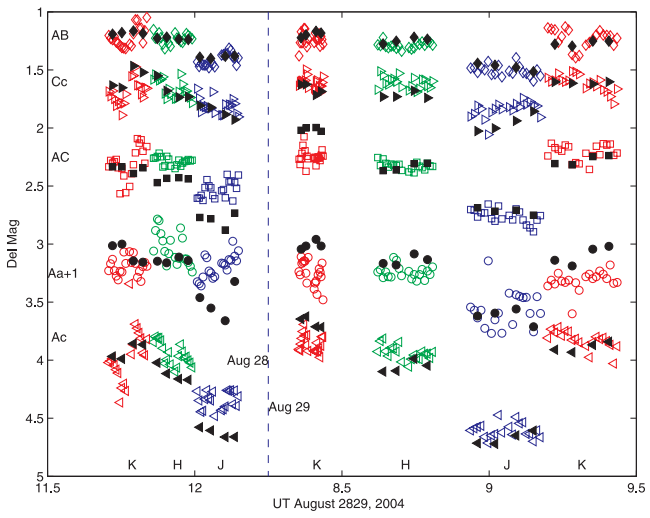

FIG. 2.—Magnitude differences for the components of ι Cas from MFBD (*filled symbols*) and PBD (*open symbols*). The Aa magnitude difference has been raised by 1 mag for visibility.

TABLE 2
WDS 00310+2839 Apparent Magnitudes

Component	Class	$T_{\rm eff}$	B (0.450 μm)	V (0.550 μm)	J (1.238 μm)	H (1.656 μm)	K_s (2.150 μm)
B	A8	7685	12.04 ± 0.28	11.81 ± 0.17	11.34	11.25	11.20
A + a	...	...	12.12 ± 0.30	11.19 ± 0.22	...	...	...
A	K1	4970 ± 230	12.70 ± 0.30	11.64 ± 0.23	10.40 ± 0.02	10.04 ± 0.02	9.95 ± 0.02
a	F5	6490 ± 670	13.07 ± 0.30	12.36 ± 0.23	11.97 ± 0.03	11.79 ± 0.04	11.72 ± 0.02

motion between the components to within the measurement error.

3. SPECTRAL CLASSIFICATION

3.1. *WDS 00310+2839*

There are few reported observations of WDS 00310+2839, but the Tycho catalog lists a B and a V magnitude for component B and a combined B and V magnitude for Aa. Converting these to the Johnson band B and V, Table 2 shows the magnitudes for each wavelength. The temperature derived from the B component's $B - V$ of 7685 K from Zombeck (1990) indicates that it is an A8 star. Using this component as a reference, we can use each of the magnitude differences at each wavelength between B and components A and a to find the apparent magnitudes shown in Table 2 and then use these to fit for a blackbody temperature and thus a spectral class.

First, we perform a blackbody fit for components A and a with just the magnitudes from Table 1 at infrared wavelengths, which also gives a predicted B and V magnitude for each. However, rather than use these individual magnitudes, we use the projected magnitude difference between components A and a, together with the Tycho combined magnitudes at these wavelengths, to derive a B and V magnitude for each. These latter magnitudes are compared with the Tycho magnitudes of the B component and added to the magnitude differences from Table 1 to derive a new blackbody temperature. Figure 3 shows the blackbody curve for the B component and the blackbody fits for components A and a.

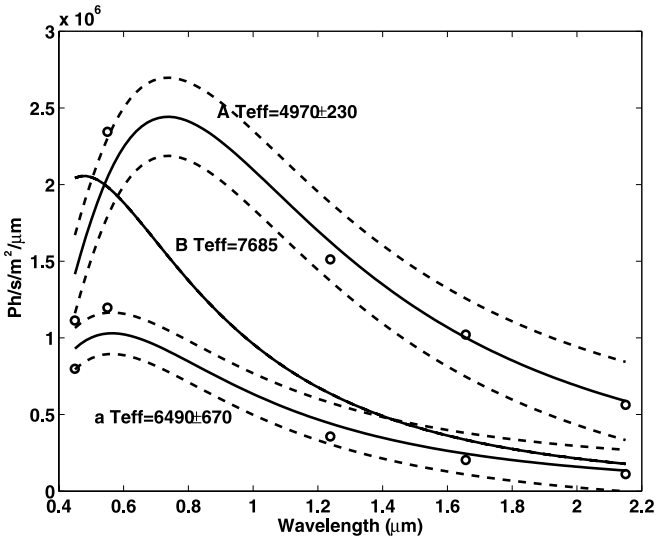

Fig. 3.—Blackbody curves for WDS 00310+2839. Component B is used as reference for the observed magnitudes for components A and a, with its temperature derived from Tycho's $B - V$ color index. The blackbody fits are shown for components A and a. For stars at the same distance, a cooler star will have less flux at every wavelength than a hotter star. Thus, component A must be a foreground object, and components B and a are the more likely gravitationally bound pair.

Of the three stars in WDS 00310+2839, component A is the brightest, yet the coolest. Therefore, it must be a foreground object, and surprisingly, it appears that the newly discovered component a is attached to component B rather than to A. From their temperatures in Figure 3, A appears to be a K1 star, and component a appears to be an F5 star. For main-sequence stars, the apparent V magnitudes and distance moduli for components B and a yield distances of 736 and 670 pc, respectively, while A appears to be at 122 pc. To be at 700 pc like components B and a, A would have to be 3.8 mag fainter, and this would imply that A is an earlier type evolved giant. However, if they are coeval, this in turn would imply that components B and a should be evolved but still does not result in an H-R diagram that makes sense. Figure 4 shows the H-R diagram using the distance modulus from the B component and applying this to components A and a.

3.2. ι *Cas*

We approach the spectral classification of the C and c components of ι Cas in the same way, using the B component, an F5 star with an appropriate temperature of 6540 K (Zombeck 1990), as a reference. All components were classified by their magnitudes at various wavelengths by Drummond et al. (2003), including the unresolved C component, but because we now split C, we repeat the analysis. As in Table 2, Table 3 contains the component apparent magnitudes calculated from the measured magnitude differences and the blackbody curve of component B rather than from the color indices listed by Zombeck. This is because the wavelengths of our filters are not quite the same as

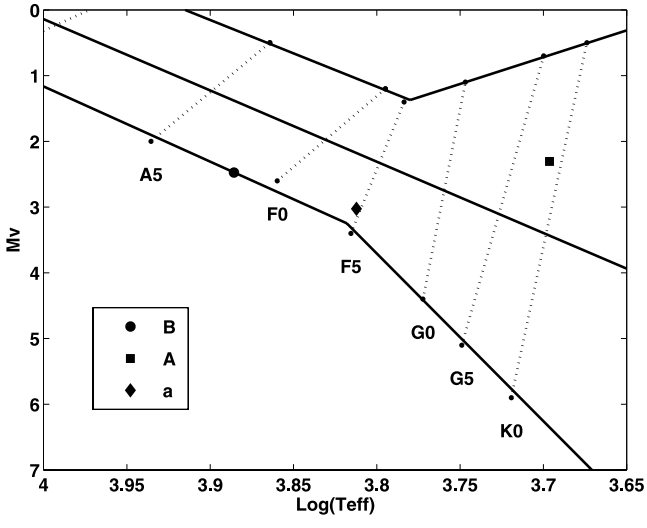

Fig. 4.—H-R diagram for WDS 00310+2839. The top, middle, and bottom solid lines mark luminosity classes III, IV, and V, respectively. Spectral types are connected across the luminosity classes with dotted lines and are labeled along the main sequence, luminosity class V. Assuming component B to be a main-sequence star with a temperature of 7685 K, components A and a are placed in the H-R diagram (*squares*) with the distance modulus of B. If all of the stars are coeval, then components B and a should have evolved more than A, again implying that A is a foreground object.

TABLE 3
ι Cas Apparent Magnitudes

Component	Class	$T_{\rm eff}$	B (0.450 μm)	V (0.550 μm)	J (1.238 μm)	H (1.656 μm)	K_s (2.150 μm)
B	F5	6540	7.30 ± 0.02	6.87 ± 0.02	6.09	5.95	5.87
A + a	(A5p)	...	4.71 ± 0.02	4.62 ± 0.01	...	...	...
A	B9 (A3)	11900 ± 550	4.72 ± 0.17	4.65 ± 0.11	4.64 ± 0.02	4.70 ± 0.01	4.65 ± 0.01
a	K1 (G6)	5070 ± 140	9.28 ± 0.17	8.63 ± 0.11	7.10 ± 0.02	6.83 ± 0.02	6.81 ± 0.13
C + c	(K3)	...	...	9.05 ± 0.06	...	...	...
C	K4	4520 ± 20	...	9.14 ± 0.10	7.39 ± 0.02	7.05 ± 0.06	6.88 ± 0.01
c	M2	3590 ± 45	...	11.84 ± 0.10	9.24 ± 0.07	8.72 ± 0.10	8.50 ± 0.02

Note.—Spectral types in parentheses from Drummond et al. (2003).

the standard astronomical filters. The blackbody fits are shown in Figure 5, with additional points at I ($\lambda = 0.9$ μm) and H (1.65 μm) supplied by the B − A and B − a magnitudes measured by Drummond et al. (2003). The magnitude difference for their unresolved C is so discrepant that it is not used in the fit, and Tycho does not contain a B magnitude for C.

Our results for ι Cas differ from the analysis of Drummond et al. (2003; the spectral types in parentheses in Table 3) because we combined new data at J, H, and K for all of the stars with Tycho data to fit each star for a blackbody temperature rather than rely on color indices from fewer wavelengths (I and H bands). Furthermore, the C component was observed only at I and was not resolved. We find then that the a component is of a later type and A is earlier. This is because we find the magnitude of unresolved components from the magnitude difference predicted by the blackbody curves and the observed combined magnitude, whereas Drummond et al. (2003) used the combined magnitude and the projected magnitude of component a to deduce the magnitude of A. The latter resulted in a brighter V magnitude for component a. All of the components are plotted in the H-R diagram—using the *Hipparcos* distance of 43.4 pc for A, a, and B, and 23.7 pc for C and c—in Figure 6.

4. STREHL RATIOS AND ANISOPLANATISM

The performance of an AO system is typically given by the Strehl ratio, which is the ratio of the peak intensity of the AO-compensated PSF to that of the ideal unaberrated PSF when both are normalized to the same volume. While this would appear to be a straightforward calculation, its computation is problematic (Roberts et al. 2004; Christou et al. 2004b). For these data, the

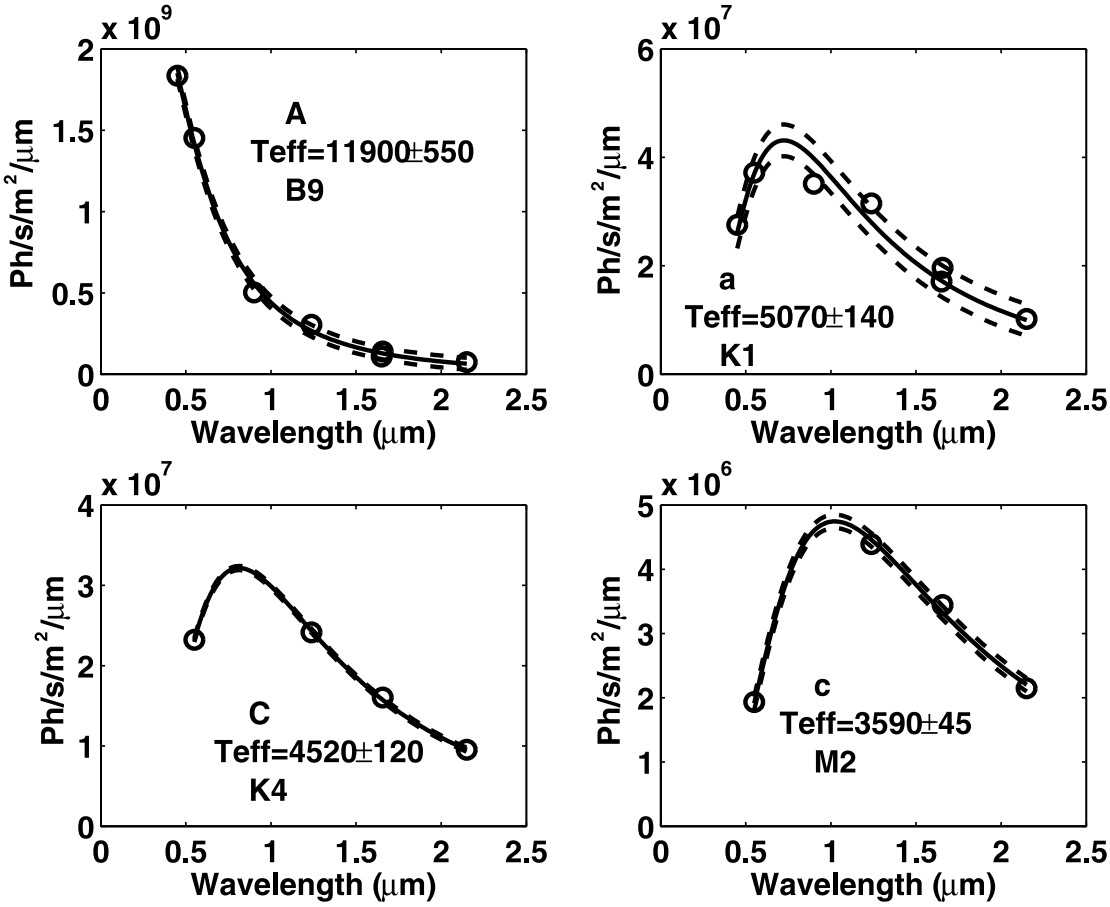

Fig. 5.—Blackbody curves for ι Cas. Component B (*not shown*) is used as the reference for the observed magnitude differences for the other components, with its temperature derived from its F5 classification and $T_{\rm eff}$ according to Zombeck (1990).

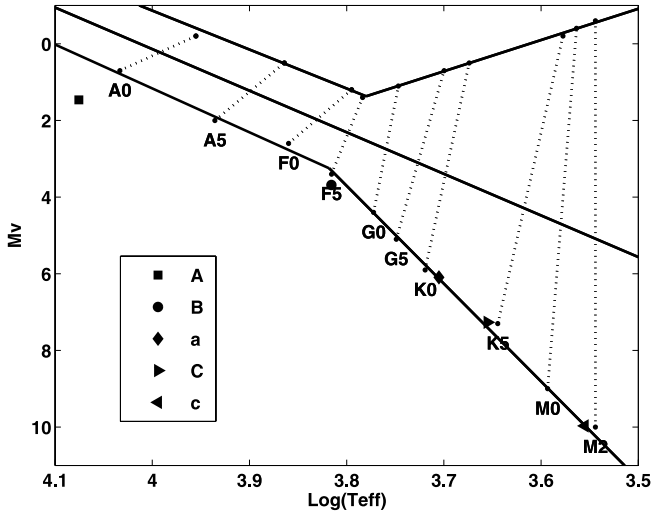

FIG. 6.—Same as Fig. 4, but for ι Cas. Assuming component B to be a main-sequence star with a temperature of 6540 K, appropriate for an F5 star, the other components are placed vertically in the figure using the *Hipparcos* distance of 43.4 pc for A, a, and B, and 23.7 pc for C and c, together with their respective magnitude differences from B, and horizontally with the temperatures derived from blackbody fits.

Strehl ratios were computed as follows. An ideal PSF for the telescope was computed numerically at an 8 times higher spatial resolution than the Nyquist-sampled data. This was done by computing an annular aperture at the corresponding pupil-plane scale using "soft" edges, i.e., by using fractional pixel intensity values when the edge of the pupil is not fully sampled by a pixel. The spiders were not modeled. The power spectrum of this annulus was computed to generate the ideal PSF. The effect of pixel binning is then simulated by binning the PSF from the original 512×512 pixel size to the final 64×64 pixel size, keeping the same field size. In order to accurately compute the Strehl ratio, the subpixel peak value needs to be determined. This was done by locating the peak pixel value and using a 5×5 pixel box surrounding this pixel to compute the centroid via a first-order moment calculation. The image was then Fourier-shifted to place the peak at the frame center. This was iterated on to a tolerance of 0.02 pixels. The Fourier-interpolated measured PSF and the ideal PSF were then normalized to have the same power within a radius of 25 pixels (1.″9). This aperture was determined by investigating the images to ascertain when the noise floor was reached.

Figure 7 shows the *K*-band Strehl ratios for each of the components of the calibration binaries, 70 Oph, σ CrB (two nights), and γ Del. The *K*-band data were used because of the undersampling at the shorter wavelengths. As can be seen from Figure 7, the Strehl ratios vary considerably during the course of the observations, but the two components track the changes together, with the off-axis component having a lower Strehl ratio for all cases. The difference in Strehl ratio between the on- and off-axis components reflects the anisoplanatism in the observations. The ratio of these two measurements is related to the size of the isoplanatic angle by the following approximation (Roddier 1999):

$$\frac{S_{\text{off-axis}}}{S_{\text{on-axis}}} \cong \exp\left[-(\theta/\theta_0)^{5/3}\right], \tag{1}$$

where θ is the angular separation of the two sources and θ_0 is the isoplanatic angle. Using this relationship we computed the isoplanatic angle for each of the three observations, given in Table 4. As can be seen, there is a range in values, but since these data were taken at different times under different conditions, this is not unexpected. The changing observing conditions are characterized by the Fried parameter r_0, which was estimated from the AO system itself using the residual wave front error

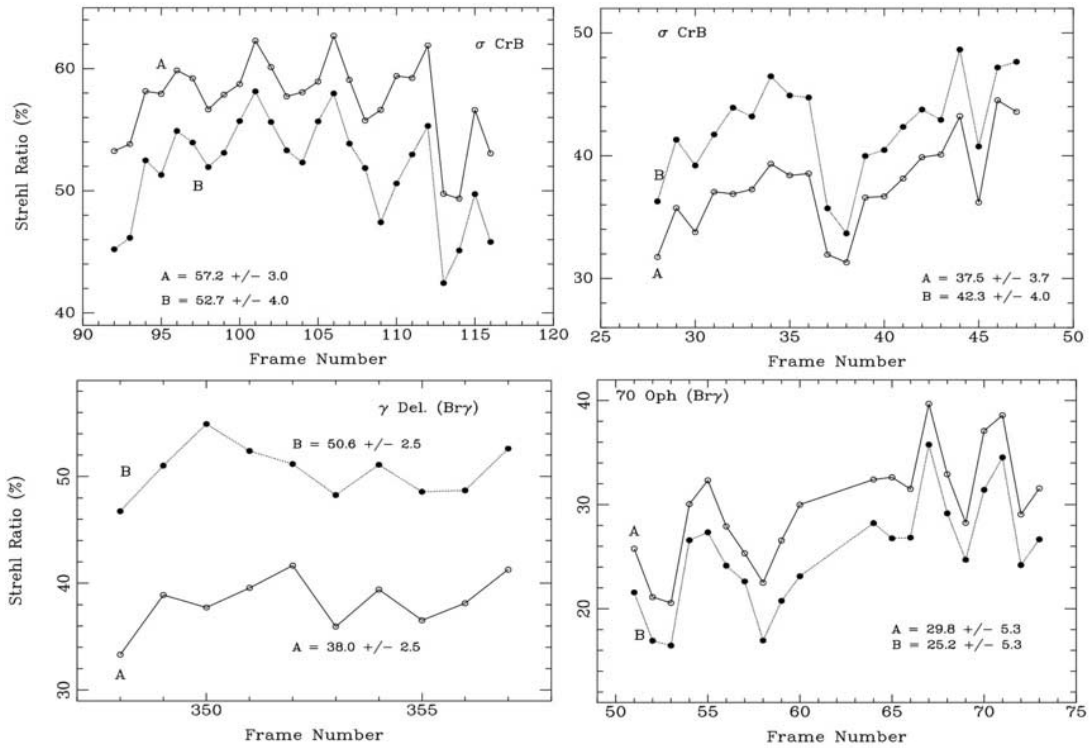

FIG. 7.—Strehl ratio measurements for the two components of each of the three calibration binary stars σ CrB (night 1, *top left*; night 2, *top right*), γ Del (*bottom left*), and 70 Oph (*bottom right*).

TABLE 4
THE ATMOSPHERIC PARAMETERS FOR THE CALIBRATION BINARIES

Star	ζ (deg)	S_{on} (%)	S_{off} (%)	θ (arcsec)	θ_0 ($\lambda = 2.2$ μm) (arcsec)	r_0 ($\lambda = 2.2$ μm) (cm)	$\bar{h}$ (km)
70 Oph (2)	35	29.8 ± 5.3	25.2 ± 5.3	4.785	14.0 ± 2.9	47	1.8
σ CrB (1)	24	57.5 ± 3.4	51.7 ± 4.2	7.032	27.2 ± 2.3	79	1.7
σ CrB (2)	20	42.3 ± 4.0	37.5 ± 3.7	7.032	25.0 ± 2.7	71	1.7
σ CrB (3)	21	47.9 ± 7.7	42.1 ± 8.8	7.032	24.1 ± 4.6	118	2.9
γ Del (1)	30	50.6 ± 2.5	38.0 ± 2.5	9.224	19.5 ± 1.3	82	2.4

NOTES.—θ_0 is computed from the on- and off-axis Strehl ratios, and both θ_0 and r_0 have not been corrected for zenith angle. The number in parentheses after the star name indicates on which of the three nights the observations were made.

based on the actuator offsets, i.e., $\sigma_a \sim 1.01(D/r_0)^{5/3}$ (D. Gavel 2005, private communication). As expected, the Strehl ratios, in general, increase with increasing r_0. Knowledge of both r_0 and θ_0 permit an estimate to be made of the mean turbulence height using the relationship (Hardy 1998)

$$\bar{h} = 0.314(\cos\zeta)\frac{r_0}{\theta_0}, \qquad (2)$$

where ζ is the zenith angle. This crude determination of the mean turbulence height suggests that it lies in the 1.5–3 km range, which compares favorably with the 2 km obtained by Steinbring et al. (2002) for Mount Hamilton. These results demonstrate how anisoplanatism can be determined from Strehl ratio measurements of calibration binary stars and can be used to build up databases for different observatories. More thorough and systematic investigations of anisoplanatism are best done using crowded fields, such as globular clusters, which permit multiple baselines to be measured simultaneously under identical atmospheric conditions (Steinbring et al. 2002).

We also investigated whether the parametric modeling of the PSFs can be used to determine the anisoplanatism. The PBD analysis fits two-dimensional elliptical Lorentzian profiles to the components. As discussed earlier, the widths of the Lorentzians were allowed to vary for separations greater than 1″. The off-axis sources had larger Lorentzian widths than the on-axis sources, as illustrated in Figure 8, which plots the mean Lorentzian radii as a function of the separation from the on-axis sources, not only for the calibration binaries but also for the close components of the multiple systems for which Strehl ratios could not be directly measured because of the presence of the close companions. As the core gets wider, the Airy rings disappear, and the Strehl ratio decreases, the Lorentzian becomes a better fit to the PSF. Figure 9 compares the measured Strehl ratios to the corresponding

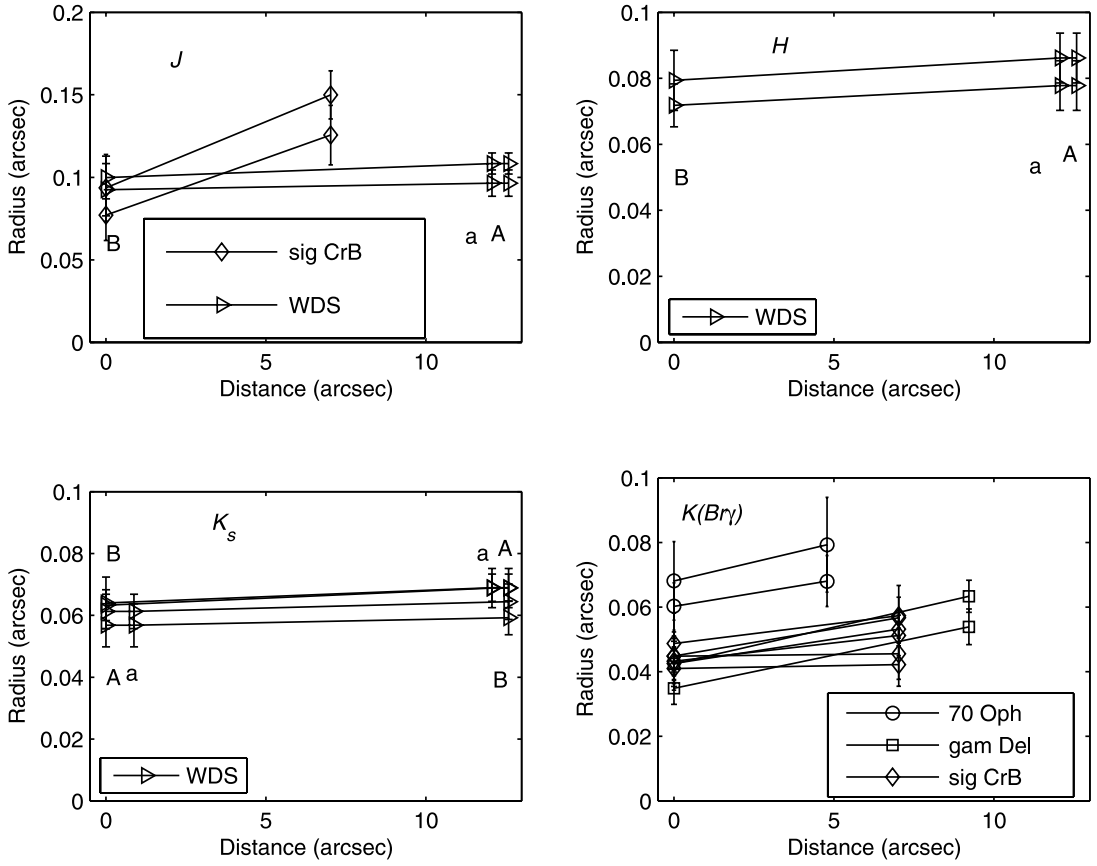

FIG. 8.—Variability in Lorentzian radii for the calibration binaries and the targets at different wavelengths. The off-axis stars have a larger Lorentzian width than the on-axis stars.

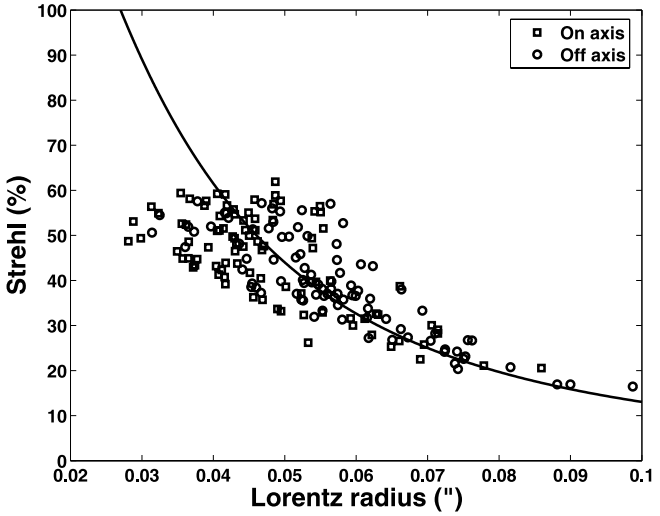

FIG. 9.—Variability in Lorentzian radii with Strehl ratio for both the on- and off-axis components of the calibration binaries. The solid line is a quadratic fit of the form $b(100/S - 1) = L^2 - 0.027^2$, where $b = 0.001391 \pm 0.000029$ and the model is anchored to a Lorentzian radius of $L = 0''.027$ when $S = 100\%$, obtained by fitting the ideal PSF.

Lorentzian model fits. These data were fitted by a quadratic relationship relating the Strehl ratio, or peak intensity, to the square of the Lorentzian radius, corresponding to the volume of the PSF. The fit was anchored at the 100% Strehl ratio value by the Lorentzian fit to the ideal PSF. As can be seen from the plot, there is considerable scatter as the image quality improves, illustrating the limitation of the single-parameter fit to the PSF as the Airy component of the PSF becomes stronger. We would expect that comparison of the Strehl ratio to the parameters of a combined fitting function (such as the ratio of the strength of the Airy component to the Lorentzian component) would reduce this scatter, and this is an avenue for future analysis.

5. PRECISION AND ACCURACY OF THE RELATIVE ASTROMETRY

A thorough investigation of the relative astrometry of the calibration binaries showed that the relative separation of the two components of each binary depended on the location of the stars on the detector, as illustrated in Figure 10 for different observations of the calibration binary σ CrB. The object was observed three separate times in $K(\mathrm{Br}\gamma)$ over the three nights. For each set of observations, the star was placed onto two separate locations on the detector so that sky data could be obtained for background calibration. The different image brightnesses (displayed on a logarithm scale), due to different exposure times, represent the three different nights the object was observed. With two nodding positions per night, a total of six different positions are obtained. The effective exposure times per frame were 200, 500, and 300 ms for nights 1, 2, and 3, respectively. The separations were obtained from the same analysis that produced the Strehl ratio measurements in the previous section, using centroiding around the brightest pixel followed by Fourier-shifting iterations. The orientation of the binary and its position on the detector produced less variation in x-axis position as compared with y-axis position, and this is reflected in the differences in the y-separations in Figure 10 (*right*). The precision of the separations for the multiple images at each position is $\sim$2 mas based on the standard deviations, corresponding to 0.03 pixels, which is on the order of the peak-fitting tolerance of 0.02 pixels, or 1.5% of a diffraction spot width. This indicates the high precision that can be achieved with AO imaging. However, comparison of the separations for the six different positions (as indicated by the x-y location of the primary) shows a dispersion in the y-separation of less than a pixel, $\sim$50 mas, or one-third of the diffraction spot, a factor of 25 larger than the precision for each observation set.

These measurements indicate a residual nonlinearity in the spatial calibration of the IRCAL detector that is sub-diffraction-limited but still significant. The image with the secondary close to the bottom of the detector shows the strongest y-separation difference, suggesting that measurements made close to the edge of the detector suffer the greatest distortion. Ignoring this data point, the y-separation dispersion is reduced to $\approx$21 mas, 15% of the diffraction spot width, which is most likely why this second-order term has not been reported before. These image scale variations indicate that careful calibration of combined camera/detector spatial scales is important if the full potential of relative astrometric measurements from AO imaging is to be reached. We note that preliminary results from recent spatial calibration

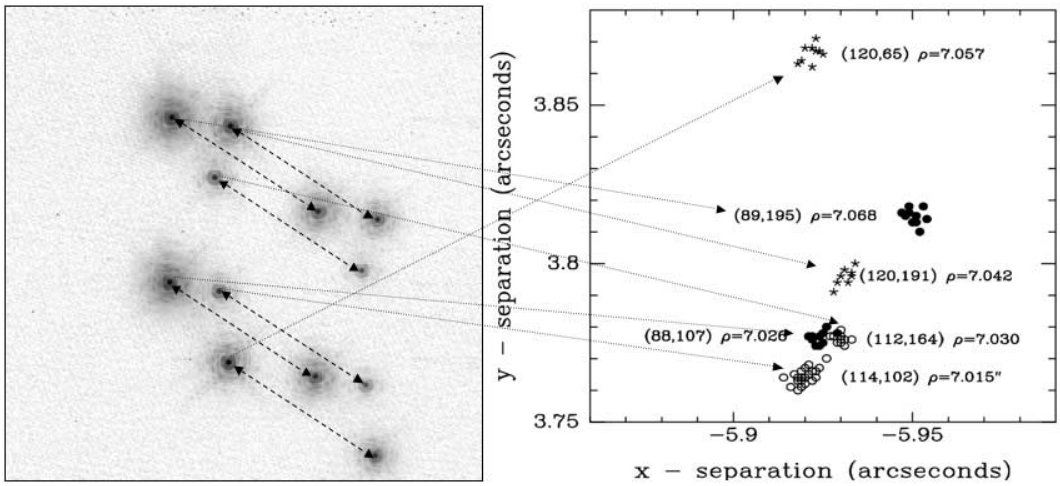

FIG. 10.—Effect on the separation vector for the calibration binary star σ CrB as its position on the detector varies. The full detector field is shown in the left panel with the six different positions of the binary (*arrows*). The relative offset ρ of the two components is plotted for the individual frames for each position along with the (x, y)-coordinates of the primary star in pixel units on the detector (*right*).

measurements confirm these spatial scale variations in the *x*- and *y*-directions, with differential image scale being more significant for the latter (M. Fitzgerald 2005, private communication).

6. SUMMARY

We have observed a number of calibration and program binaries in natural guide star (NGS) mode with the Lick Observatory adaptive optics (AO) system at the Shane 3 m telescope. From these we have been able to demonstrate that we can obtain high-precision relative astrometry to within a few milliarcseconds, equivalent to a few percent of the diffraction limit, as well as differential photometry to within a few hundredths of a magnitude. We have detected two previously unknown companions, in the multiple system ι Cas and in the binary system WDS 00310+2839. The former is a close companion to the C component, and measurements taken at Lick in 2004 and 2005, as well as a marginal detection from 2002 data (Drummond et al. 2003), imply that the components are closing. Further measurements over the next few years are required to confirm whether this is a bound companion of ι Cas C or a line-of-sight object. Our measurements of ι Cas Aa are in agreement with predictions from the previously published orbit (Drummond et al. 2003). Combining the near-infrared measurements from these observations with previously reported shorter wavelength observations and the *Hipparcos* distances have allowed us to classify the components. The components of the WDS 00310+2839 system appear to show no convincing orbital motion between 2003 September and 2005 October. Using the relative photometry reported here, as well as previously published measurements for this system, we have also fitted blackbody curves to the three components. Physically meaningful results from this analysis imply that A and a are not at the same distance and that the A component is a foreground object compared to B and a, which are at similar distances. Further observation of this system will be required to determine whether proper motions support this conjecture.

In addition to the astrophysics, we have also been able to use the binary star measurements as a probe to investigate the performance of the AO system. Anisoplanatism, PSF variability across the field, is due to different compensation in different directions across the field. Using Strehl ratio measurements of the critically sampled *K*-band images of the wide binaries, we have been able to determine an estimate of the isoplanatic angle for the site. Of course, this changes with atmospheric conditions, and measurements obtained at different zenith angles, azimuths, and times of night do not necessarily define a global measure of the isoplanatic angle. However, when combining these θ_0 estimates with corresponding r_0 estimates, we have been able to obtain estimates of the mean turbulence height (1.5–3 km) above Mount Hamilton that agree favorably with previous measurements of $\sim$2 km (Steinbring et al. 2002). The turbulence profile over continental sites is generally not modeled by the simple assumption of a single dominant layer, and it would be advantageous to have Cn^2 profiles of the site to more thoroughly investigate the measured anisoplanatism and the distribution of the turbulence. These profiles would also permit us to investigate the effect of scintillation on the variation in instantaneous differential magnitude measurements.

In obtaining these binary measurements, we compared two quite different techniques that have yielded very similar results, indicating the robustness of the parametric fitting as a quick and effective tool for extracting the binary parameters. This is a continuation of a previous study of the analysis of binary star observations with AO using data obtained from the Starfire Optical Range 3.5 m telescope under much poorer seeing conditions and consequently poorer compensation (Barnaby et al. 2000). For those data, the PSF was much better modeled with a Lorentzian, and there was no significant Airy component in the PSFs.

We have demonstrated that careful calibration of NGS AO PSFs can yield sufficient astrometric precision to allow us to determine hitherto unknown significant systematic variations in the image scale of the detector. We have also demonstrated that meaningful astrophysical quantities can be obtained from the photometry in conjunction with measurements at different wavelengths. Finally, we note that these measurements were taken with NGS AO with Strehl ratios ranging from 30% to 60%. There is every reason to expect that the same can be achieved routinely with sodium laser guide star observations at similar Strehl ratios.

We would like to thank the staff of Lick Observatory, in particular Elinor Gates, the AO Support Scientist, for her valuable assistance with the AO system, and also acknowledge many useful discussions with Donald Gavel. This work has been supported by the National Science Foundation Science and Technology Center for Adaptive Optics, managed by the University of California at Santa Cruz under cooperative agreement AST 98-76783.

REFERENCES

Barnaby, D., Spillar, E., Christou, J. C., & Drummond, J. D. 2000, AJ, 119, 378
Bauman, B. J., et al. 1999, Proc. SPIE, 3762, 194
Christou, J. C., & Drummond, J. D. 2005, in Proc. 2005 AMOS Technical Conference (Wright-Patterson AFB: AFRL)
Christou, J. C., Pugliese, G., Köhler, R., & Drummond, J. D. 2004a, PASP, 116, 734
Christou, J. C., et al. 2004b, in Proc. 2005 AMOS Technical Conference (Wright-Patterson AFB: AFRL)
Drummond, J. D. 1998, Proc. SPIE, 3353, 1030
Drummond, J. D., Milster, S., Ryan, P., & Roberts, L. C., Jr. 2003, ApJ, 585, 1007
Hardy, J. W. 1998, Adaptive Optics for Astronomical Telescopes (New York: Oxford Univ. Press)
Lauer, T. R. 1999, PASP, 111, 1434
Lloyd, J. P., Liu, M. C., Macintosh, B. A., Severson, S. A., Deich, W. T., & Graham, J. R. 2000, Proc. SPIE, 4008, 814
Mighell, K. J. 2005, MNRAS, 361, 861
Roberts, L. C., Jr., et al. 2004, Proc. SPIE, 5490, 504
———. 2005, AJ, 130, 2262
Roddier, F. 1999, Adaptive Optics in Astronomy (Cambridge: Cambridge Univ. Press)
Steinbring, E., et al. 2002, PASP, 114, 1267
Zombeck, M. V. 1990, Handbook of Space Astronomy and Astrophysics (2nd ed.; Cambridge: Cambridge Univ. Press)